Journal of
Applied
Crystallography
ISSN 1600-5767

Received 18 October 2013
Accepted 3 March 2014

Structure evolution with Sr content of the perovskite-like materials $La_{2-x}Sr_xCoTiO_6$ ($0 \leq x \leq 0.5$)

Alejandro Gómez-Pérez,[a]* Juan Carlos Pérez-Flores,[a] Clemens Ritter,[b] Khalid Boulahya,[c] German R. Castro,[d,e] Flaviano García-Alvarado[a] and Ulises Amador[a]*

[a]Quimica Facultad de Farmacia, Universidad CEU-San Pablo, Carretera de Boadilla km 5.300, Boadilla del Monte, Madrid 28668, Spain, [b]Institut Laue–Langevin, 6 Rue J. Horowitz, Grenoble, Isere/Rhone-Alpes, 38042, France, [c]Química Inorgánica, Facultad de Ciencias Químicas, Universidad Complutense de Madrid, Avenida Complutense s/n, Madrid 28040, Spain, [d]SpLine Spanish CRG Beamline, ESRF, 6 Rue J. Horowitz, Grenoble, Isere/Rhone-Alpes, 38042, France, and [e]Instituto de Ciencia de Materiales de Madrid–ICMM/CSIC, Sor Juana Inés de la Cruz 3, Madrid 28049, Spain. Correspondence e-mail: alejandro.gomezperez@ceu.es, uamador@ceu.es

The oxide series $La_{2-x}Sr_xCoTiO_6$ ($0 \leq x \leq 1.0$) belong to the perovskite family with general formula ABO_3. The evolution of the room-temperature structure as a function of the Sr content was studied using complementary techniques by applying the symmetry-adapted modes formalism (*AMPLIMODES*). In the compositional range presented in this article ($0 \leq x \leq 0.5$), the compounds adopt distorted perovskite structures of monoclinic (space group $P2_1/n$) or orthorhombic (space group *Pnma*) symmetry, both with octahedral tilting scheme ($a^-a^-c^+$) (out of phase along two perovskite main directions and in phase along the third direction). The main difference between these structures is the existence of rock-salt order of *B* ions in the monoclinic symmetry, which is lost for $x \geq 0.30$. As the Sr content increases, a better matching of the *A*—O and *B*—O distances occurs. This is produced by an elongation of the *A*—O distance as La^{3+} is replaced by the larger ion Sr^{2+}, and the shortening of the *B*—O distance due to the oxidation of Co^{2+} to Co^{3+} induced by the aliovalent substitution. As a result, the cuboctahedral *A*-site cavity becomes less and less distorted; the *A* ion tends to occupy its ideal positions, increasing its coordination and giving rise to a more symmetrical structure. In the whole compositional range, the symmetry-adapted atomic displacements (modes) responsible for the out-of-phase tilting of the BO_6 octahedra remain active but those associated with the in-phase tilting become negligible, anticipating for $x \geq 0.6$ a transition to a new structure with tilting scheme either ($a^0a^0c^-$) (space group $I4/mcm$) or ($a^-a^-a^0$) (space group *Imma*) or ($a^-a^-a^-$) (space group $R\overline{3}c$).

1. Introduction

Perovskite-like oxides with formula ABO_3 (or the more complex double perovskites with composition $AA'BB'O_6$) are very versatile materials from the point of view of composition, structure and properties (Mitchell, 2002; Ishihara, 2009; Orlovskaya & Browning, 2004), which makes them potentially useful for many applications.

In particular, they have a paramount relevance in the field of electrochemical devices such as solid oxide fuel cells (SOFCs). Many perovskite oxides are stable in oxidizing and reducing conditions at high temperatures, showing high electronic and/or ionic conductivity. Thus, some of them are currently used as SOFC components, namely electrodes, electrolytes and interconnectors. In an electrolyte, ion conduction dominates, whereas electronic conductivity should be as low as possible; for interconnectors and electrodes the opposite holds. Besides, good electrodes should also present an adequate catalytic activity (Liu *et al.*, 2007; Sun *et al.*, 2009). Some perovskite-like oxides may present these properties since they simultaneously contain cations with mixed oxidation states and anionic (oxygen) vacancies (Adler, 2004; Fergus, 2006; Ishihara *et al.*, 2004; Mitchell, 2002; Trofimenko & Ullmann, 1999). Thus, a convenient doping strategy, either in the *A* or in the *B* sites, would allow modification of the oxidation states of *B* cations as well as the creation of mobile oxygen vacancies inducing mixed (ionic and electronic) conduction. In the framework of our research on materials for SOFCs, we explored several perovskite-like oxides (Maupoey *et al.*, 2012; Pérez-Flores *et al.*, 2012, 2013). In particular we prepared the family of compounds with compositions $La_{2-x}Sr_xCoTiO_6$ ($0 \leq x \leq 1.0$), in which different structures are observed depending on the Sr content (Yuste *et al.*, 2011).

As is well known, perovskites are prone to undergo phase transitions driven by different variables such as temperature, pressure and composition (Mountstevens *et al.*, 2003; Zhao *et al.*, 2009; Khomchenko *et al.*, 2013). Although different types of phase transitions exist, they can be classified into two main categories: (*a*) those mostly due to structural distortions produced by correlated atomic displacement, which lowers the symmetry of the parent structure (displacive transitions), and (*b*) those with a dominant order–disorder component with a symmetry-breaking change of the occupation probabilities of some atomic sites (order–disorder transitions).

Since the development of the Landau theory (Landau & Lifshitz, 1959; Tolédano & Toléadano, 1987) the best formalism to deal with phase transition has been that of symmetry-adapted modes, where a mode is considered to be a collective and correlated atomic displacement fulfilling specific symmetry properties. Distorted structures can be understood as the result of a symmetry-breaking distortion of a parent structure (the aristotype with the highest possible symmetry) produced by the condensation of one or more basis modes. Thus, structural distortions in low-symmetry perovskites can be decomposed into contributions from different basis modes. Each mode consists of an amplitude and a set of atomic normalized displacements within a primitive unit cell. The atomic displacements for a given mode form its so-called polarization vector, with symmetry properties given by an irreducible representation (irrep). Within one irrep one or more basis modes can be contained. The linear combination of all the basis modes provides the nature and magnitude of the structural distortion. The basis modes can be classified into two categories: primary and secondary. A primary mode has large amplitude and is sufficient to explain the observed symmetry breaking in the transition from the high-symmetry aristotype to the low (actual)-symmetry structure. However, although the primary modes are the main cause of the observed (distorted) structure, all basis modes, except the fully symmetric one, contribute to the symmetry breaking. If none of the isotropy groups of any single irrep has the same symmetry as that observed in the distorted structure, then two or more primary modes are needed to explain the symmetry. On the other hand, secondary modes present small amplitudes (even negligible) and are coupled with primary modes. Thus, the atomic displacements due to secondary modes are very subtle, and these modes only add small displacements to the atomic positions generated by the primary modes. However, they must be considered and refined to get the actual structural parameters. All the theoretical foundations of this formalism for treating distorted structures are well documented in the literature (Howard & Stokes, 1998; Cowley, 1980; Perez-Mato *et al.*, 2010; Dove, 1997).

Besides the obvious advantages of this procedure, very convenient for crystallographic purposes, it suggests a natural hierarchy among the families of compounds, giving extra information about the physical mechanisms that induce structural distortions and stabilize the distorted phases. From a practical point of view, the use of this formalism for structure refinement using powder diffraction data is a very robust, versatile and reliable procedure. In particular, this approach avoids the situation where the refinement process gets trapped in local minima, a common drawback of the conventional Rietveld method, ensuring that the best structural model is obtained. Even more, as in the present case, the mode decomposition formalism makes it possible to compare structures with different symmetry since the primary modes are essentially equivalent in both phases.

In spite of these advantages, the mode decomposition formalism has not been commonly used because it requires a deep knowledge of group theory and complex calculations must be performed for every particular case to obtain the mode decomposition. However, the development of new free computational tools with an adequate crystallographic parameterization of the mode decomposition [*ISODISPLACE* (Campbell *et al.*, 2006) and *AMPLIMODES* (Orobengoa *et al.*, 2009)] has significantly reduced the time and effort needed to apply this approach. The symmetry-adapted modes formalism is nowadays fully implemented in some software used for structure refinement (Rodríguez-Carvajal, 1993), providing deep and detailed descriptions of structures and phase transitions of complex materials (Iturbe-Zabalo *et al.*, 2012; Iturbe-Zabalo, Igartua, Faik *et al.*, 2013; Iturbe-Zabalo, Igartua, Larrañaga *et al.*, 2013; Guzmán-Afonso *et al.*, 2011; Colin *et al.*, 2012).

The room-temperature structure of the series of compounds $La_{2-x}Sr_xCoTiO_6$ ($0 \leq x \leq 1.0$) as a function of the Sr content was determined using complementary techniques [synchrotron radiation high-resolution powder diffraction (SR-HRPD) and neutron powder diffraction (NPD)], applying the symmetry-adapted formalism for the structure refinement. High-resolution electron microscopy (HREM) and electron diffraction were used to confirm the structural models obtained. Several compositionally driven phase transitions were found; for the sake of conciseness, the study will be presented in two parts. In this first article, we report the results for the compositions in the range $0 \leq x \leq 0.5$. A second study will be published in due course.

2. Experimental

2.1. Samples

Samples of compositions $La_{2-x}Sr_xCoTiO_6$ ($0 \leq x \leq 0.5$) were prepared by a modified Pechini method from high-purity $Co(CH_3COO)_2{\cdot}4H_2O$ (Aldrich, 99.99%), La_2O_3 (Aldrich, 99.9%), $SrCO_3$ (Aldrich 99.9%) and TiO_2–anatase (Aldrich, purity 99.9%) as previously reported (Yuste *et al.*, 2011).

2.2. Experimental techniques

The purity of the samples was determined by powder X-ray diffraction (XRD) on a Bruker D8 high-resolution diffractometer, using monochromatic Cu $K\alpha_1$ (λ = 1.5406 Å) radiation obtained with a germanium primary monochromator, and equipped with a solid-state rapid LynxEye detector.

SR-HRPD patterns were collected on SpLine, the Spanish CRG beamline BM25A at the European Synchrotron

Radiation Facility (ESRF), Grenoble (France). The monochromator is a pseudo-channel-cut with two fixed Si(111) crystals moved together by a simple goniometer circle, in the $(-n, +n)$ configuration. The first monochromator crystal is ethanol-cooled while the second crystal is kept at room temperature. The second crystal is equipped with a piezoelectric driver that allows the Bragg angle to be changed very slightly (pitch adjustment) in order to reduce the harmonic content of the beam, if necessary, and to keep the transmission of the monochromator constant during long time intervals. Also, a bender curves the second crystal sagittally in order to focus the beam at the sample position (Rubio-Zuazo *et al.*, 2013). The sample was finely ground and loaded into a 0.4 mm-diameter capillary mounted in a spinning goniometer. Room-temperature data were collected in a continuous 2θ scan mode from 7 to 48° using an incident wavelength of 0.62100 (6) Å [calibrated with NIST SRM 640c silicon powder; a = 5.431195 (9) Å]. The counts from the different channels were re-binned to produce an equivalent normalized step scan of 0.01 step intervals, with a count time of 1 s per step. NPD experiments at room temperature were performed on the high-resolution diffractometer D2B at the Institut Laue–Langevin. A monochromatic beam of wavelength 1.5940 Å was selected with a Ge monochromator from the primary beam, the divergence of which was defined by an additional 10′ collimator to increase the instrumental resolution. The structural refinements were carried out by the Rietveld method by the simultaneous fitting of SR-HRPD and NPD data, using the *AMPLIMODES* formalism (Perez-Mato *et al.*, 2010, Orobengoa *et al.*, 2009) implemented in the *FullProf* program (Rodríguez-Carvajal, 1993). The neutron scattering amplitudes used in the refinement were 0.824, 0.702, 0.249, −0.344 and 0.581 (10^{-12} cm) for La, Sr, Co, Ti and O, respectively.

Selected area electron diffraction and HREM were performed using a JEOL 3000 field emission gun electron microscope, fitted with a double tilting goniometer stage (±25°, ±25°). Simulated HREM images were calculated by the multislice method using the *MacTempas* software package (R. Kilaas, Total Resolution, Berkeley, CA, USA).

Table 1
Structural parameters of the perovskite aristotypes given in both the high-symmetry (with rock-salt order of B ions, space group $Fm\bar{3}m$, and cation disordered, space group $Pm\bar{3}m$) and the low-symmetry settings (space groups $P2_1/n$ and $Pnma$, respectively), and the corresponding transformation matrixes for the high- to the low-symmetry phases.

Aristotype structures

Space group: $Fm\bar{3}m$ Cell parameter 7.8667 Å, Z = 4					Space group $Pm\bar{3}m$ Cell parameter 3.9129 Å, Z = 1				
Atom	Wyckoff position	x	y	z	Atom	Wyckoff position	x	y	z
La/Sr	8*c*	$\frac{1}{4}$	$\frac{1}{4}$	$\frac{1}{4}$	La/Sr	1*b*	$\frac{1}{2}$	$\frac{1}{2}$	$\frac{1}{2}$
Ti	4*a*	0	0	0	Co/Ti	1*a*	0	0	0
Co	4*b*	$\frac{1}{2}$	$\frac{1}{2}$	$\frac{1}{2}$	O	3*d*	$\frac{1}{2}$	0	0
O	24*e*	0.242767	0	0					

↓ ↓

$P2_1/n$ $Pnma$

$$\left(\begin{array}{ccc|c} \frac{1}{2} & \frac{1}{2} & 0 & \frac{1}{4} \\ -\frac{1}{2} & \frac{1}{2} & 0 & \frac{1}{4} \\ 0 & 0 & 1 & 0 \end{array}\right) \qquad \left(\begin{array}{ccc|c} 1 & 0 & 1 & \frac{1}{2} \\ 1 & 0 & -1 & \frac{1}{2} \\ 0 & 2 & 0 & 0 \end{array}\right)$$

↓ ↓

Low-symmetry structures

Cell parameters a = 5.5626, b = 5.5626, c = 7.8667 Å, β = 90.00°, Z = 2					Cell parameters a = 5.534, b = 7.826, c = 5.534 Å, Z = 4				
Atom	Wyckoff position	x	y	z	Atom	Wyckoff position	x	y	z
La/Sr	4*d*	0	0	$\frac{1}{4}$	La/Sr	4*c*	0	$\frac{1}{4}$	0
Ti	2*c*	0	$\frac{1}{2}$	0	Co/Ti	4*b*	$\frac{1}{2}$	0	0
Co	2*a*	0	$\frac{1}{2}$	$\frac{1}{2}$	O1	8*d*	$\frac{3}{4}$	0	$\frac{1}{4}$
O1	4*d*	0.242767	0.742767	0	O2	4*c*	0	$\frac{3}{4}$	$\frac{1}{2}$
O2	4*d*	0.757233	0.742767	0					
O3	4*d*	0	$\frac{1}{2}$	0.242767					

3. Results

3.1. Samples

Conventional X-ray diffraction data (not shown) revealed that most batches of the different compositions are single-phase and well crystallized samples. However, in some cases for the high-Sr compositions small amounts (*ca* 3% weight) of Co_3O_4 and/or CoO and $SrTiO_3$ (*ca* 3% weight) are present.

3.2. Unit-cell and symmetry determination

The complementary use of SR-HRPD and NPD data for simultaneous data fitting and structure refinement provides a powerful tool to fully determine the structural features of perovskite-like oxides. Indeed, the high peak-to-peak resolution given by SR-HRPD (even laboratory XRD provides sufficient resolution, better than that of NPD) allows the determination of the unit cell of the material that, eventually, could be distorted, this effect being reflected in the diffraction patterns as subtle peak splitting. Distortions of the unit cell are also related to changes in symmetry that could be difficult to detect if one only uses techniques with insufficient resolution. As in other studies (García-Martín *et al.*, 2004), TEM and HREM provide crucial information to develop the correct structural model or to confirm the models proposed on the basis of other techniques.

As stated above, we used *AMPLIMODES* to treat our diffraction data. The mode decomposition formalism considers any distorted structure as resulting from the distortion of a virtual aristotype structure through a series of collective displacements of atoms. The starting information on the actual ('distorted') structure is the space group, the unit cell and the number of formula units in the unit cell (Z). A model for the virtual aristotype structure is also needed. For perovskite-like structures two aristotype models can be considered (Table 1):

(1) one with rock-salt ordering of cations on the perovskite B sites and disordering in the A sites (space group $Fm\bar{3}m$) and

Table 2
Unit-cell parameters and symmetry determined for the $La_{2-x}Sr_xCoTiO_6$ ($0 \leq x \leq 0.5$) perovskites.

	X-ray source	Space group	a (Å)	b (Å)	c (Å)	β (°)
La_2CoTiO_6	Synchrotron	$P2_1/n$	5.5551 (2)	5.5781 (2)	7.8572 (2)	90.002 (9)
$La_{1.90}Sr_{0.10}CoTiO_6$	Conventional diffractometer	$P2_1/n$	5.5532 (2)	5.5656 (2)	7.8499 (2)	90.005 (9)
$La_{1.80}Sr_{0.20}CoTiO_6$	Synchrotron	$P2_1/n$	5.5502 (2)	5.5484 (2)	7.8377 (1)	90.01 (1)
$La_{1.70}Sr_{0.30}CoTiO_6$	Synchrotron	$Pnma$	5.5294 (2)	7.8187 (3)	5.5433 (2)	–
$La_{1.50}Sr_{0.50}CoTiO_6$	Synchrotron	$Pnma$	5.4919 (1)	7.7701 (2)	5.5301 (1)	–

(2) one having a cation disorder on the A and B sites (space group $Pm\bar{3}m$).

Different high-symmetry models are needed because *AMPLIMODES* cannot deal with order–disorder phase transitions. These models have been adapted to the unit-cell volume of our materials using the tools available in the Bilbao Crystallographic Server (Aroyo, Kirov *et al.*, 2006; Aroyo, Orobengoa *et al.*, 2006; Aroyo, Perez-Mato, *et al.*, 2006). At this point, high-resolution synchrotron X-ray diffraction data play a crucial role: by a Le Bail (Le Bail *et al.*, 1988) fitting of the SR-HRPD patterns a reliable unit cell and symmetry are obtained, which are used as starting information for the low-symmetry structures. Table 1 presents the unit cells of the high- and low-symmetry structures, the transformation matrices linking them, and the structural parameters of the aristotypes given in both the high- and the low-symmetry settings. All this information is used in the mode decomposition process. In Table 2 the actual cell parameters and space groups determined for our materials are presented.

From SR-HRPD data the smallest unit cell that accounts for all the reflections is the so-called diagonal perovskite cell: $a \simeq b = 2^{1/2}a_p$, $c = 2a_p$, $\alpha = \gamma = 90$ and $\beta \simeq 90°$ (a_p being the cell parameter of the cubic perovskite aristotype). This is a quite common cell in perovskite oxides. Indeed, Woodward (1997*a*,*b*) proposed several structural models with different octahedral tilting schemes for this cell which present different symmetries, from tetragonal (if $a = b$) to monoclinic (for $\beta \neq 90°$). If no cation order exists, the possible space groups are $I4/mcm$, $Imma$, $Pnma$, $I2/a$, $I2/m$ and $P2_1/m$, whereas if additional 1:1 cation order in the B sites is present the space groups are $I4/m$, $P4/mnc$, $I2/m$, $I\bar{1}$ and $P2_1/n$. By studying the systematic extinctions in the SR-HRPD (and NPD) patterns, it is possible to determine a set of space groups compatible with the experimental data. From our data the tetragonal space groups can be discarded since the a and b parameters (those that are $\sim 2^{1/2}a_p$) are significantly different (see Table 2). Figs. 1(*a*) and 1(*b*) show selected 2θ ranges of the SR-HRPD patterns for the $La_{2-x}Sr_xCoTiO_6$ compounds with $x = 0$ and $x = 0.5$, respectively. The 202, 022 and $\bar{2}02$ peaks are clearly observed for the former [monoclinic symmetry is determined (see below) for $0.0 \leq x \leq 0.2$ and the diagonal cell is oriented in such a way that $c = 2a_p$], whereas for the latter only the 220 and 022 peaks appear (for $0.3 \leq x \leq 0.5$ the diagonal cell is oriented with $b = 2a_p$ with orthorhombic symmetry). I-centred space groups can

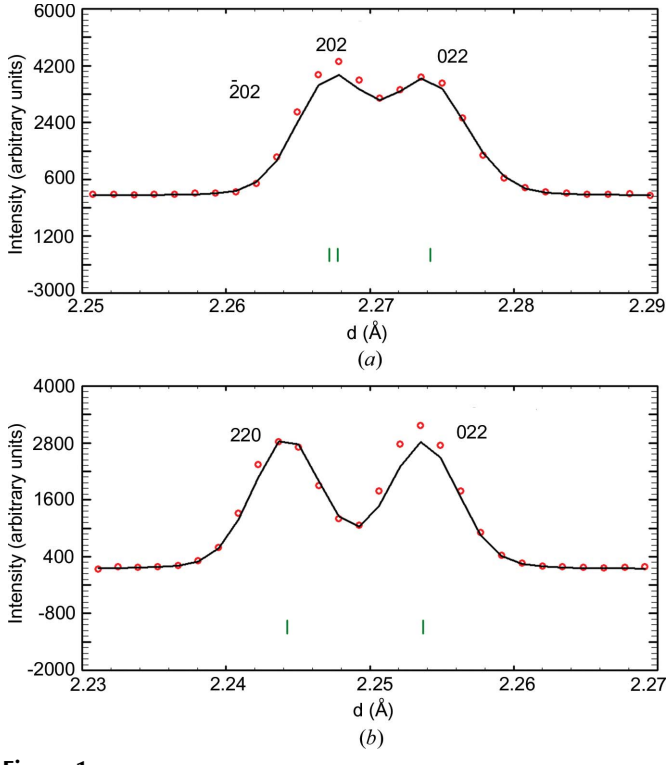

Figure 1
Expanded view of the Le Bail fitting of SR-HRPD patterns for the $x = 0$ (*a*) and $x = 0.5$ (*b*) members of the $La_{2-x}Sr_xCoTiO_6$ series, showing peaks that allow a tetragonal space group to be ruled out (see text).

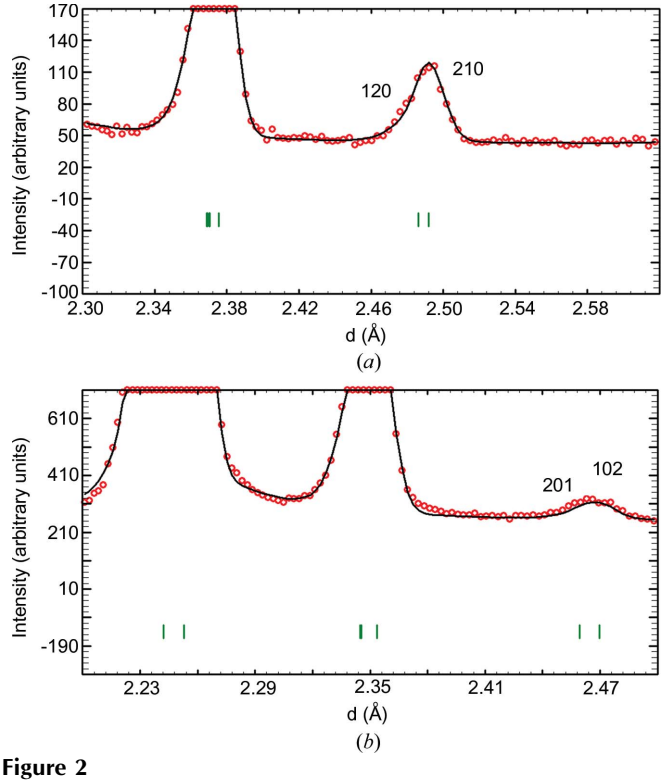

Figure 2
Expanded view of the Le Bail fitting of NPD patterns for the $x = 0$ (*a*) and $x = 0.5$ (*b*) members of the $La_{2-x}Sr_xCoTiO_6$ series, showing peaks with $h + k + l \neq 2n$, which rule out any I-centred space group (see text).

be ruled out because of the presence of the 120 and 210 peaks in the monoclinic cell and their equivalent ones, 201 and 102, in the orthorhombic cell; these peaks are relatively strong for the whole Sr-content range. Figs. 2(*a*) and 2(*b*) depict these peaks in the NPD patterns for $x = 0$ and $x = 0.50$, respectively.

At this point, the only possible symmetries are *Pnma* and $P2_1/m$ for a cationic disordered structure and $P2_1/n$ if rock-salt cationic order exists. In fact, the only difference between *Pnma* and $P2_1/n$ is the split of the *B*-site perovskites in the latter (not possible in the former), which allows 1:1 cationic ordering in the *B* sites; the tilting scheme is the same in these two space groups. In this connection, in a previous article (Pérez-Flores *et al.*, 2012) we determined that, for low levels of replacement of La^{3+} by Sr^{2+} in $La_{2-x}Sr_xNiTiO_6$, the Ni and Ti ions remain ordered (at least partially) for degrees of aliovalent substitution up to 20%, *i.e.* for values of $x \leq 0.20$. The ordered and disordered structures can be described within a diagonal cell in the space groups $P2_1/n$ and *Pnma*, respectively. Thus, we assume these space groups as a starting point for the analysis of our diffraction data. The actual value of x at which the change from orthorhombic to monoclinic symmetry occurs has been determined by trial and error, *i.e.* we used both models; the disappearance of *B*-ion order was used as a signature of the orthorhombic symmetry.

As the unit cell and space group are unambiguously determined, the transformation matrices from the aristotype ($Fm\bar{3}m$ for the *B*-ordered materials or $Pm\bar{3}m$ for the disordered ones) to the actual symmetry can be calculated; they are given in Table 1.

Using the information on the symmetries of the aristotype and the distorted structures and the transformation matrix, *AMPLIMODES* calculates the basis mode decomposition.

The starting amplitudes of the modes are obtained *ab initio* from the integrated intensities of the NPD patterns extracted by the Le Bail method (Le Bail *et al.*, 1988), which are used in a 'simulated-annealing' iteration. The use of good starting amplitudes for the modes makes the refinement process noticeably robust, avoiding the problem of being trapped in a local minimum.

Finally, as indicated in the *Experimental* section the structure refinement was performed by simultaneous fitting of the SR-HRPD and NPD patterns, the refined structural parameters being the amplitudes of each individual mode.

Table SI 1[1] collects the final atomic parameters, while in Table SI 2 selected structural information is presented. The graphical results of the fitting of SR-HRPD and NPD data are depicted in Figs. SI 1 and SI 2, respectively.

3.3. Crystal structures

3.3.1. Monoclinic structure ($0.0 \leq x \leq 0.2$). The mode decomposition of the $Fm\bar{3}m \rightarrow P2_1/n$ symmetry breaking and the refined amplitudes for the compounds $La_{2-x}Sr_xCoTiO_6$ with ($0 \leq x \leq 0.2$) are given in Tables 3 and 4, respectively. The final structure parameters are collected in Table SI 1, while selected structural information is given in Table SI 2.

Table 3
Symmetry-mode decomposition of the structure distortion from the aristotype cubic perovskite ($Fm\bar{3}m$) to the monoclinic phase ($P2_1/n$) and the atoms over which each mode acts.

Atoms	Wyckoff position	Modes
O1	24*e*	GM1+(1), GM3+(1), GM4+(1), GM5+(2), X2+(1), X3+(1), X5+(2)
La1/Sr1	8*c*	GM5+(2), X5+(1)

Seven irreducible representations can contribute to the symmetry breaking: GM1+(1) (fully symmetric), GM3+(1), GM4+(1), GM5+(4), X2+(1), X3+(1) and X5+(3) [using the notation proposed by Howard & Stokes (1998); the numbers in parentheses are the number of modes that transform according to the symmetry of the given irrep]. There are nine basis modes involving displacements of O atoms and three for *A* ions. Table 4 shows, for the $Fm\bar{3}m$ to $P2_1/n$ structure evolution, the direction of the order parameter and the propagation vector for every basis mode, the mode amplitude (in ångström), and the isotropy group (*i.e.* the symmetry that would result if the given mode were the only operating one).

The effect of every irrep mode is depicted in Fig. 3. The fully symmetric GM1+ mode is related to the relocation of the O atoms in the new sub-space: the virtual high-symmetry structure (space group $Fm\bar{3}m$) has one degree of freedom for the x parameter of oxygen (Table 1); thus, this unidimensional mode is responsible for the adjustment of the x coordinate in the new symmetry. By GM3+ the BO_6 octahedra expand in the equatorial *ab* plane, whereas the apical oxygen is displaced along the octahedron axis to its centre. The GM4+ mode describes a rotation of the octahedron around the *b* axis, which deforms the octahedron. This mode is associated with the out-of-phase tilting of the BO_6 octahedra. Four basis vectors transform according to the GM5+ irrep: two modes acting over the *A* ions and two on the O atoms. The latter displace the *A* ions along the *a* and *c* axes, whereas those acting on the O atoms define a rotation along the *b* axis with apical oxygen moving in opposite directions. The basis mode with symmetry X2+ deforms the square defined by the four equatorial O atoms into a rhombus, whereas X3+ consists of a rotation around the *c* axis. This mode is associated with octahedral in-phase tilting in perovskites. Finally, there are three modes belonging to the X5+ irrep: two of them acting on the O atoms and the third on the *A* ions. For O atoms they consist of displacements in the *ac* plane and in the *ab* plane; for *A* ions the effect is a movement along the *b* axis, this being the largest displacement of *A* cations.

Since none of the isotropy groups associated with the irreps obtained in the mode decomposition has the same symmetry as that of the distorted structure, two or more primary modes are needed to explain the actual symmetry. From Table 4 it is clear that the two primary modes are GM4+ and X3+; the secondary mode X5+ also plays an important role in the formation of the distorted structure since its amplitude is much larger than those of the other secondary modes.

[1] Supporting information for this article is available from the IUCr electronic archives (Reference: RW5065).

Table 4
Summary of the mode decomposition, after simultaneous fitting of SR-HRPD and NPD data at room temperature, for the $Fm\bar{3}m$ to $P2_1/n$ structure distortion.

GM4+ and X3+ are the primary irrep modes. Samples are indicated by their Sr content, x, in $La_{2-x}Sr_xCoTiO_6$.

					Amplitude (Å)		
K vector	Irrep	Direction	Isotropy subgroup	Dimension	x = 0.00	x = 0.10	x = 0.20
(0, 0, 0)	GM1+	(a)	$Fm\bar{3}m$	1	0.008 (8)	0.028 (6)	0.020 (4)
(0, 0, 0)	GM3+	(a, 0)	$I4/mmm$	1	0.08 (2)	0.05 (2)	0.00 (4)
(0, 0, 0)	GM4+	(a, a, 0)	$C2/m$	1	1.200 (4)	1.172 (4)	1.120 (3)
(0, 0, 0)	GM5+	($-b$, a, $-a$)	$C2/m$	4	0.081 (5)	0.105 (9)	0.074 (5)
(0, 1, 0)	X2+	(0, a, 0)	$P4_2/mnm$	1	0.002 (7)	0.016 (6)	0.007 (5)
(0, 1, 0)	X3+	(0, a, 0)	$P4/mnc$	1	0.797 (5)	0.741 (5)	0.686 (4)
(0, 1, 0)	X5+	(a, a, 0, 0, a, $-a$)	$Pnnm$	3	0.405 (3)	0.504 (3)	0.444 (3)

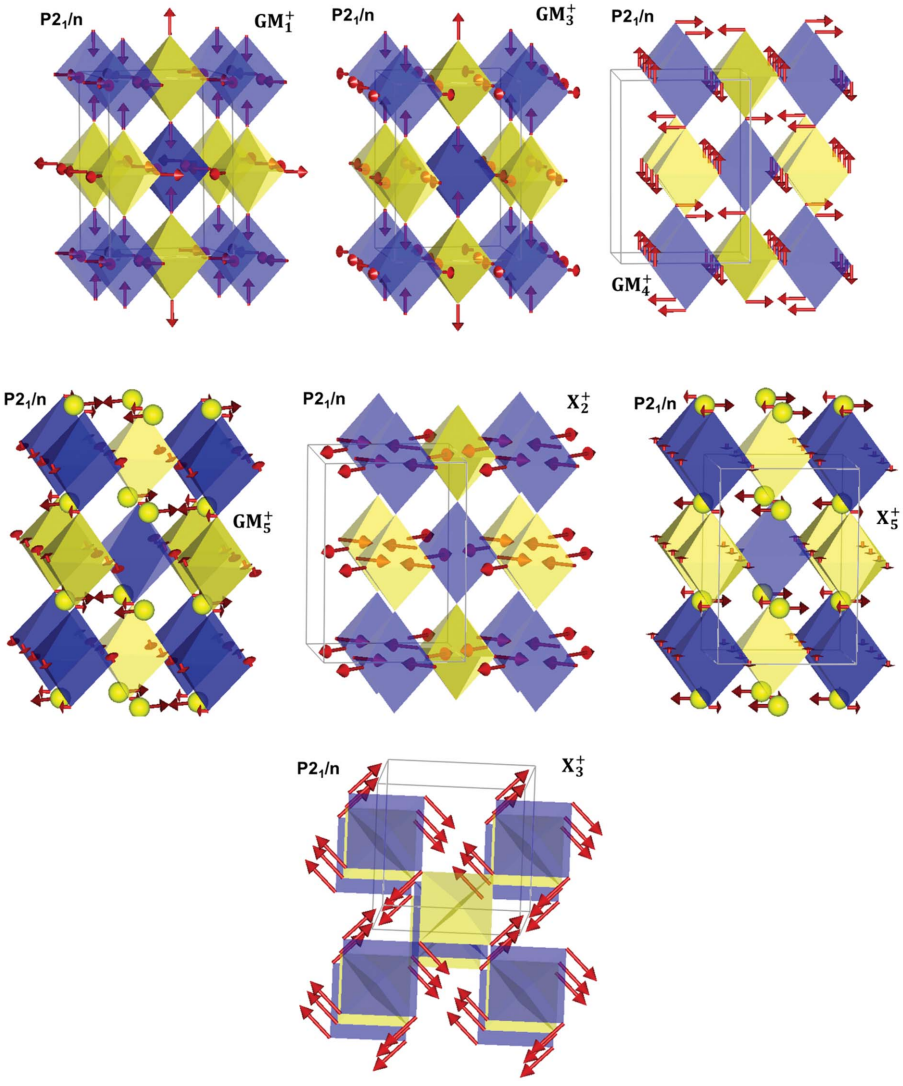

Figure 3
Schematic representation of the seven irrep modes in the $P2_1/n$ configuration: Co and Ti octahedra are shown in blue and yellow, respectively, La/Sr are shown as yellow balls, and O atoms are at the octahedron corners.

The amplitudes of the modes decrease with increasing Sr content, suggesting a release of the structure distortion. Indeed, the greater size of Sr^{2+} in comparison to La^{3+}, and the oxidation of Co^{2+} into Co^{3+} as charge-compensating mechanism (Yuste *et al.*, 2011) rendering these B ions smaller, result in a better matching of the $A-O$ and $B-O$ distances, which is reflected in the values of the tolerance factors being closer and closer to unity (Fig. 4*a*).

The observed decrease of the amplitudes of the primary modes GM4+ and X3+ is clearly associated with the decrease of the tilting angles (Fig. 4). This fact supports the idea that these modes are responsible for the octahedral tilting, being the order parameters that conduct the transition from the aristotype to the distorted structure.

To confirm the results obtained by XRD and NPD, an electron microscopy study was performed. The HREM micrograph along the $[110]_p$ (p refers to the perovskite simple cell) zone axis of $La_{1.8}Sr_{0.2}CoTiO_6$ is shown in Fig. 5. Two different zones (A and B) are clearly distinguishable: the first one with d spacings of 2.7 and 7.6 Å corresponds to the $[010]_m$ (m refers to the monoclinic diagonal cell) direction, whereas the second one showing d spacings of 5.5 and 7.6 Å corresponds to the $[100]_m$ direction. The optical Fourier transforms corresponding to the two structural domains are depicted in Figs. 5(*a*) and 5(*b*), respectively. The slight mismatch of the c_m axis (*ca* 7.6 Å) in the domain boundary between zones A and B suggests a monoclinic distortion. All the reflections in Figs. 5(*a*) and 5(*b*) can be indexed in the monoclinic unit cell $a_m = 2^{1/2}a_p$, $b_m = 2^{1/2}a_p$, $c_m = 2a_p$, $\beta \simeq 90^\circ$ and space group $P2_1/n$, supporting the results obtained by SR-HRPD and NPD. Moreover, the simulated image calculated using the structural model given in Table SI 1 fits nicely to the experimental one (see Fig. 5), confirming the rock-salt order in the perovskite B sites.

3.3.2. Orthorhombic structure ($0.3 \leq x \leq 0.5$). The modes of the transition $Pm\bar{3}m \rightarrow Pnma$ and the final amplitudes for $La_{2-x}Sr_xCoTiO_6$ with ($0.3 \leq x \leq 0.5$) are presented in Tables 5 and 6, respectively. In this case, the symmetry breaking proceeds through modes whose symmetries are given by five irreducible representations (Table 5): R4+(1), R5+(2), X5+(2), M2+(1) and M3+(1).

Table 5
Symmetry-mode decomposition of the structure distortion from the aristotype cubic perovskite $Pm\bar{3}m$ to the orthorhombic phase (*Pnma*) and the atoms over which each mode acts.

Atoms	Wyckoff position	Modes
O1	3*d*	R4+(1), (R5+1), X5+(1), M2+(1), M3+(1)
La1/Sr1	1*b*	R5+(1), X5+(1)

Table 6 presents the direction of the order parameter, the propagation vector and amplitudes (in ångström), and the isotropy group for the basis modes for the $Pm\bar{3}m$ to *Pnma* structure transition. The final refined structural model is presented in Table SI 1.

As for the previous case, an electron microscopy study of $La_{1.7}Sr_{0.3}CoTiO_6$ was performed to confirm the model obtained by XRD and NPD. The HREM micrograph along the $[110]_p$ zone axis is shown in Fig. 6. Two domains are observed (A and B): the first one with *d* spacings of 5.5 and 7.8 Å corresponds to the [100] direction, while the second domain is oriented along [010], showing *d* spacings of 2.7 and 7.8 Å. The optical Fourier transforms of the two structural domains are depicted in Figs. 6(*a*) and 6(*b*), respectively. A good matching in the domain frontier of zones A and B suggests an orthorhombic symmetry; indeed, the reflections can be indexed in the space group *Pnma* with unit-cell parameters $a_o = 2^{1/2}a_p$, $b_o = 2a_p$ and $c_o = 2^{1/2}a_p$. These results agree

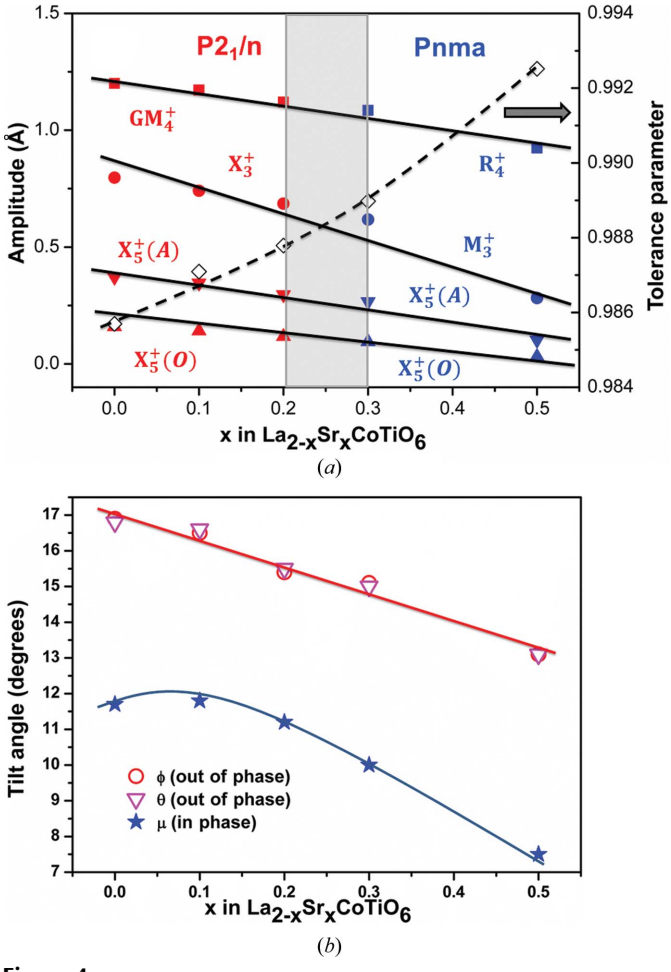

Figure 4
Evolution of the modes amplitudes and the tolerance factor (*a*) and the octahedral tilt angles (*b*) with the Sr content for $La_{2-x}Sr_xCoTiO_6$ ($0.0 \leq x \leq 0.5$). Lines are guides for the eye.

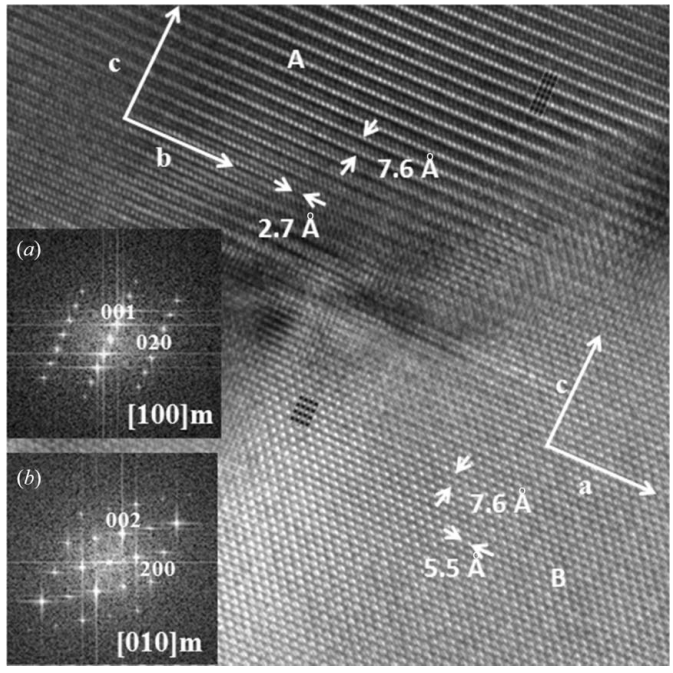

Figure 5
HREM image of $La_{1.80}Sr_{0.20}CoTiO_6$ along $[110]_p$. A twinned structure is clearly seen. (*a*), (*b*) Optical FFTs of the domains marked A and B in the image, respectively. The simulated images are seen in the insets (Δt = 5 nm and $\Delta f = -30$ nm).

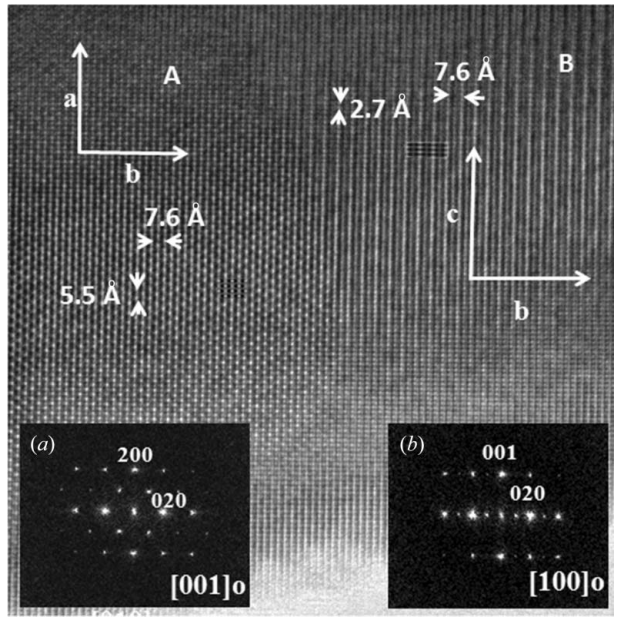

Figure 6
HREM image of $La_{1.70}Sr_{0.30}CoTiO_6$ along $[110]_p$. A twinned structure is clearly seen. (*a*), (*b*) Optical FFTs of the domains marked *A* and *B* in the image, respectively. The simulated images are seen in the insets (Δt = 5 nm and $\Delta f = -30$ nm).

Table 6
Summary of the mode decomposition, after simultaneous fitting of SR-HRPD and NPD data at room temperature, for the $Pm\bar{3}m$ to *Pnma* structure evolution.

R4+ and M3+ are the primary irrep modes. Samples are indicated by their Sr content, x, in $La_{2-x}Sr_xCoTiO_6$.

					Amplitude (Å)	
K vector	Irrep	Direction	Isotropy subgroup	Dimension	x = 0.30	x = 0.50
$(\frac{1}{2}, \frac{1}{2}, \frac{1}{2})$	R4+	$(0, a, a)$	*Imma*	1	1.085 (2)	0.9240 (18)
$(\frac{1}{2}, \frac{1}{2}, \frac{1}{2})$	R5+	$(0, a, -a)$	*Imma*	2	0.067 (4)	0.043 (3)
$(0, \frac{1}{2}, 0)$	X5+	$(0, 0, 0, -a, 0, 0)$	*Cmcm*	2	0.388 (2)	0.149 (4)
$(\frac{1}{2}, \frac{1}{2}, 0)$	M2+	$(a, 0, 0)$	*P4/mbm*	1	0.002 (5)	0.004(5)
$(\frac{1}{2}, \frac{1}{2}, 0)$	M3+	$(a, 0, 0)$	*P4/mbm*	1	0.618 (4)	0.282 (4)

with the model given in Table SI 1 that was used to calculate the image presented in Fig. 6. The good fit of this image with the experimental one supports the random distribution of *B* ions.

The irrep modes in Tables 6 and SI 1 are depicted in Fig. 7. The mode with R4+ symmetry has exactly the same effect as GM4+ in the formation of the monoclinic phase previously discussed, *i.e.* it is responsible for the out-of-phase octahedral tilting. Two basis modes transform according to the R5+ irrep: one responsible for a displacement of the *A* ion along the *a* axis and a second mode describing the motion of the O atoms, which defines a rotation around the *b* axis with opposite displacements of the apical O atoms. Also two modes belong to the X5+ irrep: the first one displacing the apical O atoms along the *b* axis, whereas the second mode moves the *A* ions in the same direction. The mode with symmetry given by M2+ displaces the O atoms in the square equatorial planes of the octahedra to transform them into a rhombus. Finally, the mode of symmetry M3+ has the same effect as symmetry X3+ in the monoclinic space group, *i.e.* this is the mode associated with the in-phase tilting of the BO_6 octahedra.

As in the $Fm\bar{3}m \rightarrow P2_1/n$ transformation, in the $Pm\bar{3}m \rightarrow$ *Pnma* symmetry breaking there exist two primary active modes: R4+ and M3+. On the other hand, although the modes belonging to the X5+ irrep are secondary ones, they make a noticeable contribution to the final structural model. These modes are strongly correlated to the M3+ one. According to Perez-Mato *et al.* (2010), strong correlations of secondary modes to primary ones suggest the presence of internal constraints in the structure and/or a common origin of the correlated modes. It is difficult to detect these structural features by a conventional Rietveld refinement. These correlations can be shown in a plot of the mode amplitudes as a function of the thermodynamic parameter (T, P, composition). Thus, two (or more) modes are correlated if their amplitudes follow the same trend. From Fig. 4(*a*) a clear correlation between the secondary X5+ and the primary M3+ modes can be seen.

On the other hand, the M3+ mode strongly decreases as the Sr content increases, whereas the R4+ mode decays more slowly. This suggests that, as the internal structural stresses are relieved as a consequence of a better matching of the $A-O$ and $B-O$ bonds, the in-phase octahedral tilting (associated with M3+) tends to disappear.

All the other modes, except R4+ which is associated with out-of-phase tilting, have amplitudes close to zero for $x = 0.5$, anticipating a completely different tilting scheme and symmetry for higher Sr contents.

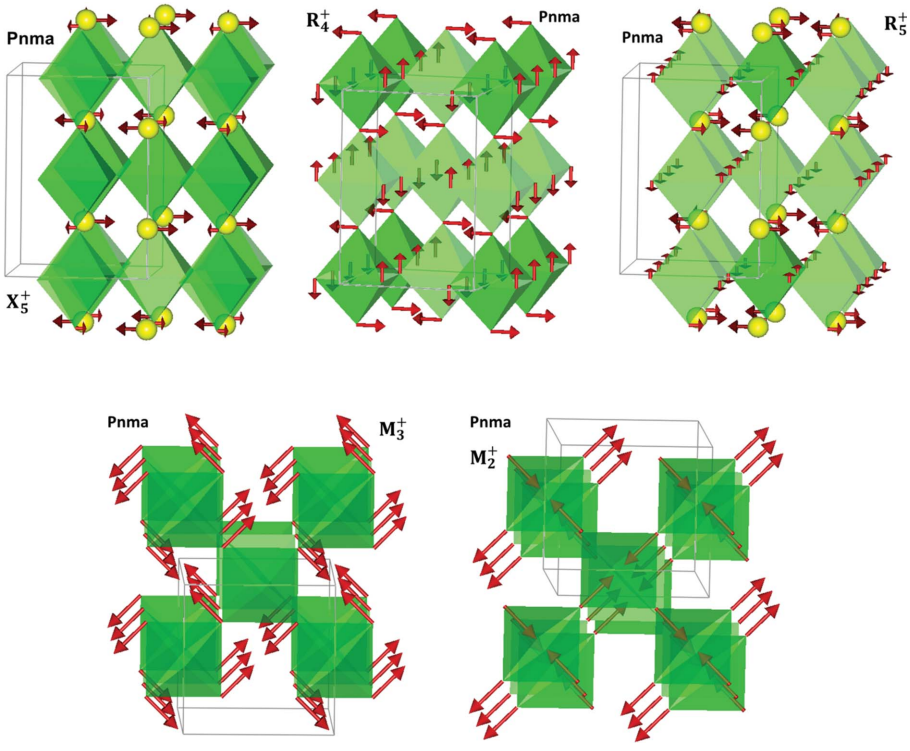

Figure 7
Schematic representation of the five irrep modes in the *Pnma* configuration: Co/Ti octahedra are shown in green, La/Sr are shown as yellow balls and O atoms are at the octahedron corners.

4. Concluding remarks

Compounds of the series $La_{2-x}Sr_x$-$CoTiO_6$ ($0.0 \leq x \leq 0.5$) adopt perovskite-like structures of monoclinic (space group $P2_1/n$) or orthorhombic (space group *Pnma*) symmetry. The main difference between the two structures is the existence of rock-salt order of *B* ions in the monoclinic symmetry, which is lost for $x \geq 0.30$. As the Sr content increases, the perovskite structure becomes more symmetrical as a consequence of a better matching of the $A-O$ and $B-O$ distances. This is produced by an elongation of the $A-O$ distance as La^{3+} is replaced by the larger ion Sr^{2+}, and the shortening of the $B-O$ distance as a result of the oxidation of Co^{2+} to Co^{3+} induced by the aliovalent substitution. These changes are reflected in the tolerance factor, which

approaches unity, providing a signature of a structure of higher symmetry.

From the *AMPLIMODES* study it is evident that the primary modes GM4+/R4+ are responsible for the out-of-phase tilt of the BO_6 octahedra. Like all the other modes, they decrease with increasing x (as the structure becomes more symmetrical), but, contrary to what happens for the other modes (X3+/X5+) which almost vanish for $x \simeq 0.5$, the GM4+/R4+ modes still present a large amplitude for this Sr content. Interestingly, X5+ seems to be strongly correlated to M3+ (which is associated with in-phase tilting). The X5+ irrep is multidimensional (twofold degenerate in $P2_1/n$ or threefold in *Pnma*). The most important contribution to the total amplitude (Tables SI 3 and SI 4) is the mode acting on the *A* ion, which displaces it from the ideal perovskite *A* site, at the centre of a cuboctahedron of O atoms, along the **y** direction. It is known that when *A* cations are too small for the cuboctahedral 12-fold-coordinated cavity the perovskite structure distorts through tilts of the BO_6 octahedra, reducing the coordination number from 12 to 8 or 9. From the evolution of this mode it is clear that as the Sr content increases the cuboctahedral cavity becomes less and less distorted, and the *A* ion tends to occupy its ideal position, increasing its coordination; as a result the symmetry of the structure increases.

The evolution of the amplitudes of the primary modes R4+ and M3+ and the secondary one X5+ with the Sr content (Fig. 4*a*) allows us to predict that a phase 'transition' occurs for $x > 0.5$. The symmetry of the new phase will be determined by the remaining primary active mode (with nonzero amplitude) R4+ associated with out-of-phase tilting of BO_6 octahedra. Therefore, as the amplitude of the M3+ mode, related to in-phase octahedral tilts, becomes negligible, the expected symmetry of the new structure will be that of the isotropy group of the mode basis of irrep R4+, *i.e.* space group *Imma* (Table 6) with tilting scheme ($a^-a^-c^0$). However, this symmetry is not common in perovskites since the orientation of the order parameter associated with the mode easily changes through a first-order phase transition. The only two possible directions are

(1) (a, 0, 0), yielding a space group $I4/mcm$ and tilting scheme ($a^0a^0c^-$), and

(2) (a, a, a) to give a tilting scheme ($a^-a^-a^-$) and space group $R\overline{3}c$.

These two possibilities can be found in the literature on temperature-driven phase transitions. $SrZrO_3$ (Howard & Stokes, 1998; Kennedy *et al.*, 1999) and $Sr_{1-x}Ba_xSnO_3$ (Mountstevens *et al.*, 2003) are examples of the tetragonal case, whereas $BaCeO_3$ (Knight, 1994) is an example of the rhombohedral symmetry.

These will be the only possibilities if no additional effects such as cation ordering, cation displacements from their ideal positions *etc.* appear as the Sr content in $La_{2-x}Sr_xCoTiO_6$ becomes higher than $x = 0.5$. A detailed study of our materials in this compositional range will be published elsewhere.

We thank the Spanish Ministerio de Ciencia e Innovación and Comunidad de Madrid for funding the projects MAT2010-19837-C06-01 and S-2009/PPQ-1626, respectively. Financial support from Universidad CEU San Pablo is also acknowledged. We acknowledge the Spanish Ministerio de Ciencia e Innovación and Consejo Superior de Investigaciones Científicas for financial support and for provision of synchrotron radiation facilities, and we would like to thank the beamline staff for their assistance in using beamline BM25-SpLine. Access to the neutron facilities at the Institut Laue–Langevin is gratefully acknowledged.

References

Adler, S. B. (2004). *Chem. Rev.* **104**, 4791–4843.
Aroyo, M. I., Kirov, A., Capillas, C., Perez-Mato, J. M. & Wondratschek, H. (2006). *Acta Cryst.* A**62**, 115–128.
Aroyo, M. I., Orobengoa, D., Capillas, C. & Perez-Mato, J. M. (2006). *Acta Cryst.* A**62**, s58.
Aroyo, M. I., Perez-Mato, J. M., Capillas, C., Kroumova, E., Ivantchev, S., Madariaga, G., Kirov, A. & Wondratschek, H. (2006). *Z. Kristallogr. Cryst. Mater.* **221**, 15–27.
Campbell, B. J., Stokes, H. T., Tanner, D. E. & Hatch, D. M. (2006). *J. Appl. Cryst.* **39**, 607–614.
Colin, C. V., Pérez, A. G., Bordet, P., Goujon, C. & Darie, C. (2012). *Phys. Rev. B*, **85**, 224103.
Cowley, R. (1980). *Adv. Phys.* **29**, 1–110.
Dove, M. T. (1997). *Am. Mineral.* **82**, 213–244.
Fergus, J. W. (2006). *J. Power Sources*, **162**, 30–40.
García-Martín, S., Alario-Franco, M. A., Ehrenberg, H., Rodríguez-Carvajal, J. & Amador, U. (2004). *J. Am. Chem. Soc.* **126**, 3587–3596.
Guzmán-Afonso, C., González-Silgo, C., González-Platas, J., Torres, M. E., Lozano-Gorrín, A. D., Sabalisck, N., Sánchez-Fajardo, V., Campo, J. & Rodríguez-Carvajal, J. (2011). *J. Phys. Condens. Matter*, **23**, 325402.
Howard, C. J. & Stokes, H. T. (1998). *Acta Cryst.* B**54**, 782–789.
Ishihara, T. (2009). Editor. *Perovskite Oxide for Solid Oxide Fuel Cells*. New York: Springer.
Ishihara, T., Ishikawa, S., Ando, M., Nishiguchi, H. & Takita, Y. (2004). *Solid State Ionics*, **173**, 9–15.
Iturbe-Zabalo, E., Fabelo, O., Gateshki, M. & Igartua, J. M. (2012). *Acta Cryst.* B**68**, 590–601.
Iturbe-Zabalo, E., Igartua, J. M., Faik, A., Larrañaga, A., Hoelzel, M. & Cuello, G. J. (2013). *J. Solid State Chem.* **198**, 24–38.
Iturbe-Zabalo, E., Igartua, J. M., Larrañaga, A., Pomjakushin, V., Castro, G. & Cuello, G. J. (2013). *J. Phys. Condens. Matter*, **25**, 205401.
Kennedy, B., Howard, C. & Chakoumakos, B. (1999). *Phys. Rev. B*, **59**, 4023–4027.
Khomchenko, V. A., Troyanchuk, I. O., Többens, D. M., Sikolenko, V. & Paixão, J. A. (2013). *J. Phys. Condens. Matter*, **25**, 135902.
Knight, K. (1994). *Solid State Ionics*, **74**, 109–117.
Landau, L. D. & Lifshitz, E. M. (1959). *Statistical Physics*. London: Pergamon.
Le Bail, A., Duroy, H. & Fourquet, J. (1988). *Mater. Res. Bull.* **23**, 447–452.
Liu, Z., Han, M. & Miao, W. (2007). *J. Power Sources*, **173**, 837–841.
Maupoey, Z., Azcondo, M. T., Amador, U., Kuhn, A., Pérez-Flores, J. C., Romero de Paz, J., Bonanos, N. & García-Alvarado, F. (2012). *J. Mater. Chem.* **22**, 18033–18042.
Mitchell, R. H. (2002). *Perovskite: Modern and Ancient.* Ontario: Almaz Press.
Mountstevens, E. H., Attfield, J. P. & Redfern, S. A. T. (2003). *J. Phys. Condens. Matter*, **15**, 8315–8326.
Orlovskaya, N. & Browning, N. (2004). Editors. *Mixed Ionic Electronic Conducting Perovskites for Advanced Energy Systems*. Kiev: Springer.

Orobengoa, D., Capillas, C., Aroyo, M. I. & Perez-Mato, J. M. (2009). *J. Appl. Cryst.* **42**, 820–833.
Pérez-Flores, J. C., Pérez-Collect, D., García-Martín, S., Ritter, C., Mather, G. C., Canales-Vázquez, J., Gálvez-Sánchez, M., García-Alvarado, F. & Amador, U. (2013). *Chem. Mater.* **25**, 2484–2494.
Pérez-Flores, J., Ritter, C., Pérez-Collect, D., Mather, G., Canales-Vázquez, J., Gálvez-Sánchez, M., García-Alvarado, F. & Amador, U. (2012). *Int. J. Hydrogen Energy*, **37**, 7242–7251.
Perez-Mato, J. M., Orobengoa, D. & Aroyo, M. I. (2010). *Acta Cryst.* A**66**, 558–590.
Rodríguez-Carvajal, J. (1993). *Physica B*, **192**, 55–69.
Rubio-Zuazo, J., Collado-Negro, V., Heyman, C., Ferrer, P., da Silva, I., Gallastegui, J. A., Gutiérrez-León, A. & Castro, G. R. (2013). *J. Phys. Conf. Ser.* **425**, 052005.
Sun, X., Wang, S., Wang, Z., Qian, J., Wen, T. & Huang, F. (2009). *J. Power Sources*, **187**, 85–89.
Tolédano, J. C. & Toléadano, P. (1987). *The Landau Theory of Phase Transitions: Application to Structural, Incommensurate, Magnetic, and Liquid Crystal Systems.* London: World Scientific Publishing Company.
Trofimenko, N. & Ullmann, H. (1999). *Solid State Ionics*, **124**, 263–270.
Woodward, P. M. (1997*a*). *Acta Cryst.* B**53**, 32–43.
Woodward, P. M. (1997*b*). *Acta Cryst.* B**53**, 44–66.
Yuste, M., Pérez-Flores, J. C., de Paz, J. R., Azcondo, M. T., García-Alvarado, F. & Amador, U. (2011). *Dalton Trans.* **40**, 7908–7915.
Zhao, J., Ross, N. L., Angel, R. J., Carpenter, M. A., Howard, C. J., Pawlak, D. A. & Lukasiewicz, T. (2009). *J. Phys. Condens. Matter*, **21**, 235403.